

Chapter 2

High- T_c SQUIDs

Superconductivity was discovered by Kamerlingh Onnes in 1911 after he succeeded in liquefying helium [1]. Kamerlingh Onnes discovered that the electrical resistance of mercury vanished when it was cooled to below 4.2 K. The transition temperature of a superconductor is known as the critical temperature, T_c , and is a material-specific property. Zero resistance is one of the characteristic properties of superconductors and the other defining property is called the Meissner effect, discovered in 1933 [2]. The characteristic of the Meissner effects is that magnetic fields are completely expelled from inside the bulk of a superconductor when cooled to below T_c . The electrons in a superconductor pair up in so-called Cooper pairs [3] due to interaction with lattice vibrations, known as phonons, that make it possible for electrons to travel through the material without dissipation.

An important breakthrough in superconducting technology came in 1986 when Bednorz and Müller discovered the first high temperature superconductor with a T_c of 35 K [4] for which they were awarded the 1987 Nobel prize in physics. Shortly after, superconductivity in $\text{YBa}_2\text{Cu}_3\text{O}_{7-\delta}$ (YBCO) was discovered [5] with $T_c = 93$ K which made it possible to use liquid nitrogen as the refrigerant. YBCO is one of the most commonly used high- T_c superconductors today and is the material used throughout this work.

The discovery of superconductivity and the high- T_c materials opened up the field for new applications. This chapter describes the development of high- T_c SQUIDs including theory, considerations, and fabrication of SQUID sensors.

For more details on superconductivity and devices see for example [6–9].

2.1 The Josephson Effect

A Josephson junction consists of two superconductors separated by a thin insulating barrier. The insulator forms a weak link that Cooper pairs can tunnel through, thus, a current can flow through the barrier without dissipation. The behavior of such a device

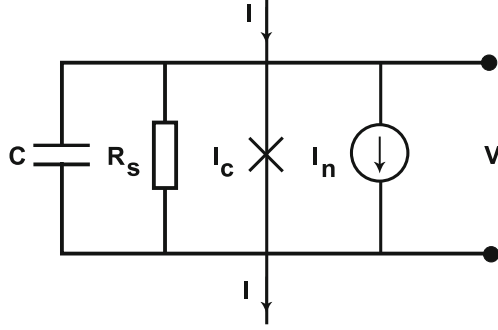


Fig. 2.1 An equivalent circuit of a capacitively (C) and resistively (R_s) shunted Josephson junction with critical current I_c and noise current I_n

was predicted by Josephson in 1962 [10] and the governing Josephson relations are:

$$I = I_c \sin \phi \quad (2.1)$$

$$V = \frac{\hbar}{2e} \frac{\partial \phi}{\partial t} = \frac{\Phi_0}{2\pi} \frac{\partial \phi}{\partial t} \quad (2.2)$$

where I_c is the critical current (the maximum supercurrent that can flow in the junction), ϕ is the phase difference across the junction, $\Phi_0 = h/2e = 2 \cdot 10^{-15}$ Wb is the flux quantum and e is the electron charge. These two equations (Eqs. 2.1 and 2.2) are referred to as the dc and ac Josephson effect, respectively.

A common way of modeling a Josephson junction is by capacitively (C) and resistively (R_s) shunting an ideal junction. This model is called the resistively and capacitively shunted junction (RCSJ) model and is shown in Fig. 2.1 [8, 11, 12]. The current flowing through the model circuit using the Josephson relations can be described by

$$I = C \frac{\Phi_0}{2\pi} \ddot{\phi} + \frac{1}{R_s} \frac{\Phi_0}{2\pi} \dot{\phi} + I_c \sin \phi + I_n, \quad (2.3)$$

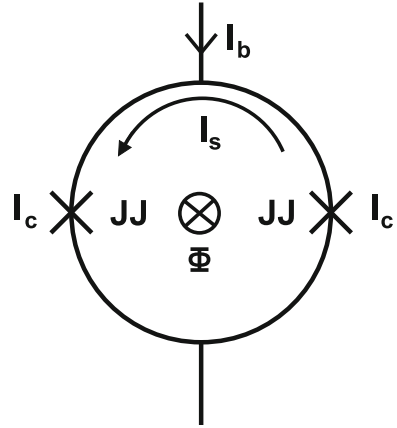
where I_n is the noise current from the shunting resistor R_s . From this model arises the Stuart-McCumber parameter:

$$\beta_c = \frac{2\pi I_c R_s^2 C}{\Phi_0}, \quad (2.4)$$

that is used as a condition for hysteresis in the junction's IV characteristics. For highly dissipative junctions used for sensors, $\beta_c < 1$.

In order to retain coupling between the two superconducting electrodes in the presence of thermal noise, the Josephson coupling energy, $I_c \Phi_0 / 2\pi$, has to be larger than the thermal noise [8, 13]. This condition is expressed as

Fig. 2.2 Schematic drawing of a dc SQUID. Two Josephson junctions (JJ) interrupt a superconducting ring. An applied magnetic flux (Φ) directed into the plane of the SQUID induces a screening current (I_s) in the ring. The screening current adds to the bias current (I_b) and alters the critical current of the junctions



$$\Gamma = \frac{2\pi k_B T}{I_c \Phi_0} \leq 1, \quad (2.5)$$

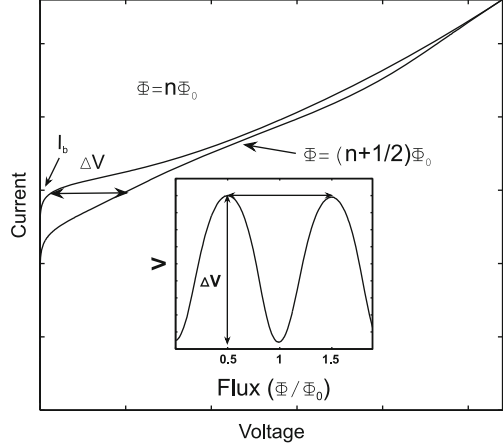
where T is the operation temperature of the junction.

2.2 The dc SQUID

A superconducting quantum interference device (SQUID) is a flux to voltage transducer and is one of the most sensitive devices for detecting magnetic fields known today. A dc SQUID is a superconducting ring interrupted by two Josephson junctions in parallel as illustrated in Fig. 2.2. An important physical effect (in a SQUID) is that the flux penetrating a superconducting ring is quantized ($\Phi = n\Phi_0$, $n = 1, 2, 3 \dots$ [7]). A typical IV -curve of a SQUID with external magnetic flux is shown in Fig. 2.3. When the SQUID is biased with a current bias I_b slightly above the critical current of the SQUID ($2I_c$) the junctions are in the resistive state. Since the critical current of the junctions is modulated with the applied magnetic flux, the output voltage will also be a function of magnetic flux as illustrated in Fig. 2.3.

The IV -curve and the operation of a SQUID can be understood from the following description. If the critical currents of the two junctions are equal, as shown in Fig. 2.2, then the bias current, I_b , will split equally in the superconducting ring. An applied magnetic flux (Φ) induces a circulating current in the ring (with inductance L) given by $I_s = -\Phi/L$. The screening current adds to the bias current through the junctions which means the critical current, as measured, decreases. As the applied flux reaches $\Phi = \Phi_0/2$ the SQUID switches into normal state and lets one flux quantum into the ring, which means I_s changes sign. At this point we are at the minimum critical current of the SQUID as indicated by the lower IV -curve in Fig. 2.3. As the flux increases to one flux quantum, the screening current decreases and the maximum

Fig. 2.3 Measured I - V -curve with varied applied flux. The applied flux reduces the critical current and consequently, a voltage modulation appears as a function of the applied magnetic flux (inset)



critical current is restored (upper I - V -curve in Fig. 2.3). If the SQUID is biased at a constant current (I_b in Fig. 2.3), this yields a voltage modulation as illustrated in the inset of Fig. 2.3.

2.2.1 Noise in dc SQUIDS

There are several types of voltage noise in SQUIDS: Nyquist noise of the Josephson junctions, thermal fluctuations of the critical current and $1/f$ flicker noise associated with motion of flux vortices in the superconducting thin film. The contribution of thermal noise in SQUIDS is more significant in high- T_c devices operating at 77 K than the low- T_c equivalent operating at liquid helium temperatures (4.2 K). If the spectral density of the voltage noise across the SQUID is S_V then the flux noise (typically quoted for SQUIDS) is given by

$$S_\Phi = \frac{S_V}{V_\Phi^2} \quad (2.6)$$

where $V_\Phi = \partial V / \partial \Phi$ is the transfer function of the SQUID. The voltage noise is generated by Nyquist noise from the dynamic resistance in the SQUID at the measurement frequency, f_m , but it is also mixed down to the measurement frequency from $f_J \pm f_m$ (where $f_J = V/\Phi_0 = 483.6 \text{ MHz}/\mu\text{V}$ is the Josephson frequency). The spectral density of the voltage noise (in the limit $\beta_c \ll 1$, $I > I_c$ and $f_m \ll f_J$) is given by [14–16]

$$S_V = \left[1 + \frac{1}{2} \left(\frac{I_c}{I_b} \right)^2 \right] \frac{4k_B T R_d^2}{R_s} \quad (2.7)$$

where the first term is the Nyquist noise generated in the dynamic resistance, R_d , and the second term represents the mixed down noise. A second effect of thermal noise is rounding of the IV -curve at low voltages due to current fluctuations [17].

Thermal noise gives several constraints on the SQUID parameters. The effect of thermal noise for coupling between the superconducting electrodes in the Josephson junctions was briefly discussed in Sect. 2.1. Computer simulations by Clarke and Koch [18] suggested an additional factor of 5, thus:

$$\Gamma = \frac{2\pi k_B T}{I_c \Phi_0} \leq 0.2. \quad (2.8)$$

For $T = 77\text{ K}$, we obtain $I_c > 17\text{ }\mu\text{A}$. For high- T_c SQUIDs one should also keep in mind that the thermally induced flux noise in the SQUID loop, $\langle \Phi_N^2 \rangle^{1/2} = (k_B T L)^{1/2}$, should be less than one flux quantum which limits the SQUID inductance [8].

The noise in the low frequency regime is usually referred to as $1/f$ noise or flicker noise. The inverse proportionality to frequency makes reduction of flicker noise important for applications where signals are measured at low frequencies, e.g. in MEG. In general, there are two sources of flicker noise. The first one comes from critical current fluctuations due to electrons getting trapped on defects in the barrier and subsequently released [19–21]. The motion of electrons as they trap and release increases the current density locally in the junction and the result is switching of the critical current randomly back and forth as the electrons are released.

The fluctuations of the critical current in the two junctions can be in-phase or out-of-phase. The in-phase component appears as voltage noise in the $V\Phi$ -curve shifting the curve in voltage whereas the out-of-phase component gives flux noise and thus a phase shift in the $V\Phi$ -curve. By using an appropriate bias scheme, both the in-phase and the out-of-phase component can be reduced substantially [22].

The other type of flicker noise arises from trapped flux that hops between different pinning sites in the superconducting film. Flux gets trapped in the superconducting film when cooled through the transition temperature in the presence of an external magnetic field and the effect is enhanced if the magnetic field is increased. Flux hopping can be reduced by patterning holes in the superconducting film preventing the flux from hopping between pinning sites [23].

2.2.2 SQUID Readout

The SQUID is operated in a flux-locked loop (FLL). The signal from the SQUID is amplified and returned to a feedback coil inductively coupled to the SQUID as shown in Fig. 2.4. The feedback coil generates a flux in the SQUID which opposes the external flux in the SQUID loop. The SQUID is flux locked where the voltage to flux modulation is the steepest in order to achieve highest sensitivity. The signal

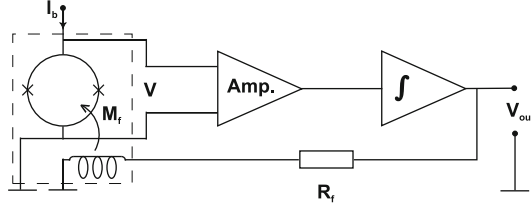
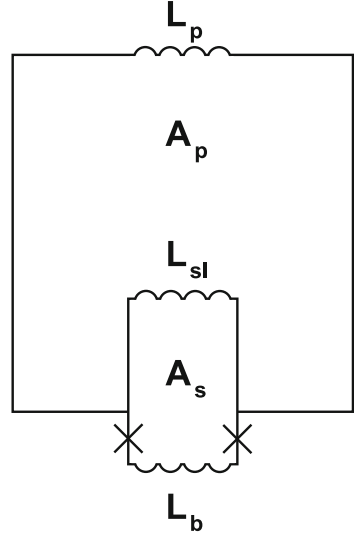


Fig. 2.4 Basic drawing of the FLL SQUID readout. The signal from the SQUID is amplified, integrated and sent back to a feedback coil inductively coupled to the SQUID. The feedback coil cancels the flux in the SQUID. Cold parts are indicated by the *dashed box*

Fig. 2.5 A schematic circuit of a directly coupled magnetometer indicating the inductances of the pick-up coil (L_p), the SQUID slit (L_{sl}), and the junction bridge (L_b). The effective area of the SQUID and the pick-up loop are A_s and A_p respectively. The Josephson junctions are indicated by crosses



fed back to the feedback coil also passes through a feedback resistor (R_f) in order to read out the signal (V_{out}).

The critical current fluctuations giving in-phase and out-of-phase fluctuations are effectively canceled by using a flux-modulated bias-reversal scheme. Bias reversal switches the polarity of the $V\Phi$ -characteristics which effectively cancels the in- and out-of-phase fluctuations while remaining sensitive to changes in the $V\Phi$ -curve due to applied magnetic flux [22].

2.2.3 SQUID Considerations

Optimization of a SQUID concerns noise, field tolerance and effective area. From simulations it was concluded that $\Gamma = \frac{2\pi k_B T}{I_c \Phi_0} \leq 0.2$ and $\beta_L = 2LI_c/\Phi_0 = 1$ [18, 24]. This puts constraints on the critical current and the SQUID inductance,

$I_c > 17 \mu\text{A}$ and $L < 59 \text{ pH}$. Simulations done by Enpuku et al. show the dependence of inductance on the noise properties of high- T_c dc SQUIDs [25] and the effect of thermal noise on the voltage modulation [26]. It was shown that the flux noise ($S_\Phi^{1/2}$) scales with the SQUID inductance for $L < 100 \text{ pH}$ and increases substantially for higher inductances.

The effective area of a directly coupled SQUID magnetometer is [27]:

$$A_{eff} = A_s + k \frac{A_p}{L_p} L \quad (2.9)$$

where $k \approx L_{sl}/L$ is a coupling constant, $L = L_{sl} + L_b$ is the SQUID inductance where L_{sl} and L_b are the SQUID slit inductance and the inductance related to the junction bridge respectively, A_s is the effective area of the bare SQUID, A_p and L_p are the effective area and inductance of the pick-up loop respectively (see Fig. 2.5). The effective area of the bare SQUID can be neglected and inserting the coupling constant gives $A_{eff} \propto A_p(L_{sl}/L_p)$. This is also reflected in the noise performance, using $V \approx R/L$ and $S_V = 16k_B T R$ [8] one obtains for the field sensitivity [28]:

$$S_B^{1/2} = \frac{S_V^{1/2}}{V_\Phi A_{eff}} \propto \frac{L}{L_{sl}}. \quad (2.10)$$

In summary, the effective area should be maximized and according to Eq. 2.10 one should minimize L/L_{sl} which was more closely investigated in [28]. The junctions should be designed such that the critical current is higher than $17 \mu\text{A}$ and the inductance of the SQUID should not be too large ($< 59 \text{ H}$). Lines in the film should be kept small in order to avoid flux hopping that causes low frequency noise [23]. Finally, the width of the junctions should be kept small enough not to reduce the critical current modulation due to coupling to magnetic fields. The expression [29]

$$\Delta B \approx \Phi_0 \frac{1.84}{\omega_j^2}, \quad (2.11)$$

where ΔB is the maximum magnetic field, and ω_j is the width of the Josephson junction can be used to estimate the maximum junction width given the amplitude of the magnetic field.

2.2.4 Device Layout

Depending on the application and experimental setup a different type of sensor layout may be needed. In the setup for MIA the SQUID sensor was operated without magnetic shielding. In order to reduce the influence of far distant sources of noise one can use a gradiometer layout. Furthermore, for MIA an excitation magnetic

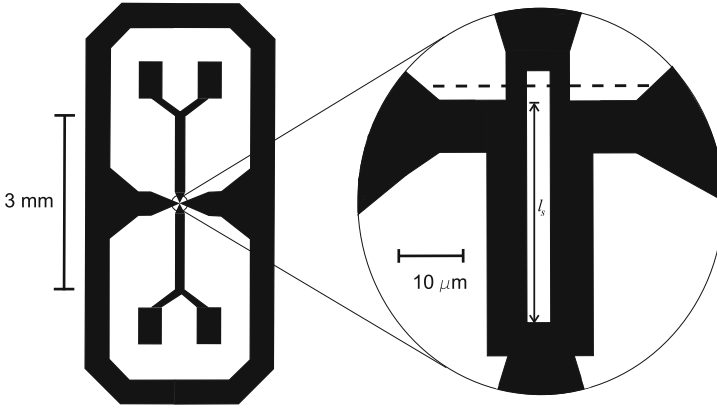


Fig. 2.6 On the *left* is the layout of GRAD1. The two pick-up loops, with width $400\ \mu\text{m}$, constitute a “figure eight”. An homogeneous applied magnetic field will induce circulating currents flowing in the same direction in the two loops. When the currents meet in the middle they cancel, thus the SQUID is blind to homogeneous magnetic fields. The baseline is $3\ \text{mm}$ as indicated, thus, the design is optimized for small sample sizes. On the *right* is the layout of the hairpin SQUID in this device. The dashed line indicates the grain boundary of the substrate creating the Josephson junctions in the superconducting ring. The SQUID slit is indicated by the length $l_s = 30\ \mu\text{m}$. The width of the slit and striplines of the SQUID are 3 and $7\ \mu\text{m}$, respectively

field was applied (see Chap. 3) using a Helmholtz coil that produced a homogeneous magnetic field in the vicinity of the SQUID. Due to these circumstances, gradiometers were more appropriate for this application. Gradiometers were also developed for the ULF-MRI setup, although the results obtained in this thesis on ULF-NMR/MRI were measured with a shielded SQUID magnetometer.

The layout of one of the fabricated SQUID gradiometers (GRAD1) is shown in Fig. 2.6. Currents induced by homogeneous magnetic fields are cancelled in the center of the “figure eight” configuration of the gradiometer since the induced currents will effectively only appear in the perimeter. The SQUID is a so-called hairpin SQUID. It has a thin SQUID slit as opposed to the typical square washer type [30].

The layout of GRAD2-5 (shown in Fig. 2.7) is similar to GRAD1 but the baseline is increased to $4\ \text{mm}$ and the SQUID inductance is higher ($60\ \text{pH}$, length of slit, width of slit, and width of striplines were 50 , 3 , and $4\ \mu\text{m}$, respectively).

GRAD6 is a single gradiometer on a $10 \times 10\ \text{mm}^2$ STO substrate. The layout, shown in Fig. 2.8 incorporates an array of 20 Josephson junctions with widths of $6\ \mu\text{m}$ to serve as flux dams in order to protect the SQUID from the high currents induced during magnetic pulses (for ULF-NMR/MRI, see Chap. 5), but also to reduce the risk of trapping magnetic flux in the thin film close to the SQUID. In addition, the linewidth of the gradiometer was reduced to $200\ \mu\text{m}$. The area of the pick-up loops was increased in this design.

For the MEG recordings, we used a magnetometer layout since the measurements were made inside a magnetically shielded room and we wanted to maximize the

Fig. 2.7 Layout of GRAD2-5. In this design, two gradiometers are fabricated on the same chip (GRAD2-3 and GRAD4-5). The baseline is increased to 4 mm and the SQUID, which is a hairpin type similar to GRAD1 (Fig. 2.6), has length of slit, width of slit, and width of striplines of 50, 3, and 4 μm , respectively. The *dashed line* indicates the grain boundary of the substrate

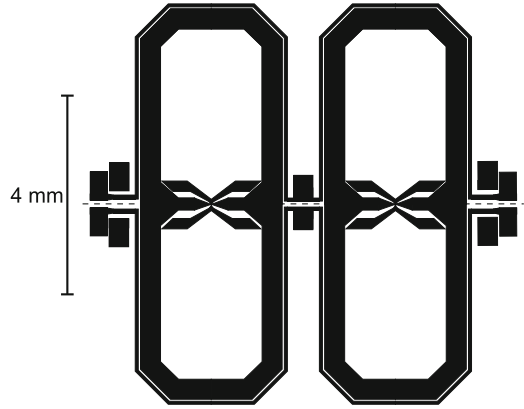
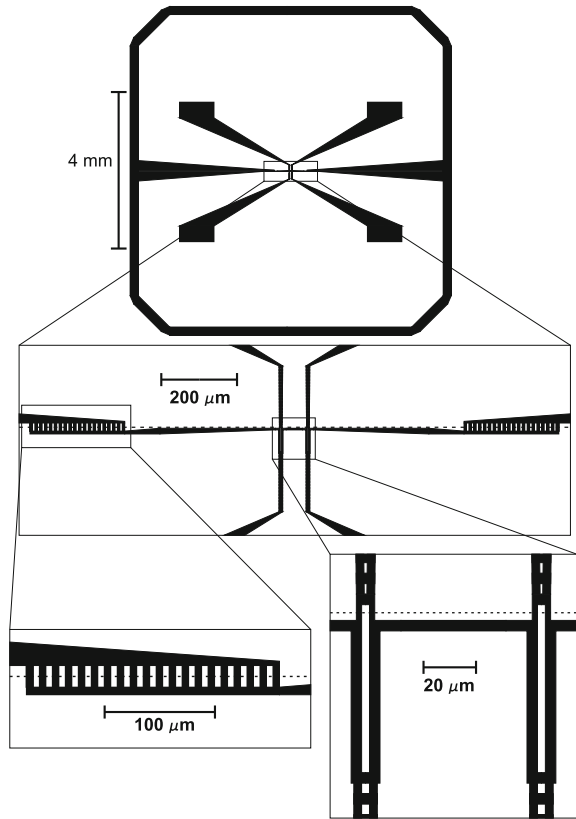


Fig. 2.8 The layout of GRAD6 shown at different scales. The *uppermost* figure shows the overall layout of the gradiometer. The middle panel shows the flux dam configuration with the two SQUIDs. The bottom left panel shows the 20 Josephson junctions that constitute the flux dam on the left side of the two SQUIDs and the bottom right panel shows the two redundant hairpin SQUIDs. The grain boundary is indicated by the *dashed line*



field sensitivity by making the area of the pick-up loop large. The layout of the magnetometer device is shown in Fig. 2.9. It has a $8 \times 8 \text{ mm}^2$ pick-up loop with a linewidth of $400 \mu\text{m}$. For redundancy and higher yield purposes, two SQUIDs were included and placed in series. The hairpin SQUIDs had the same design as in

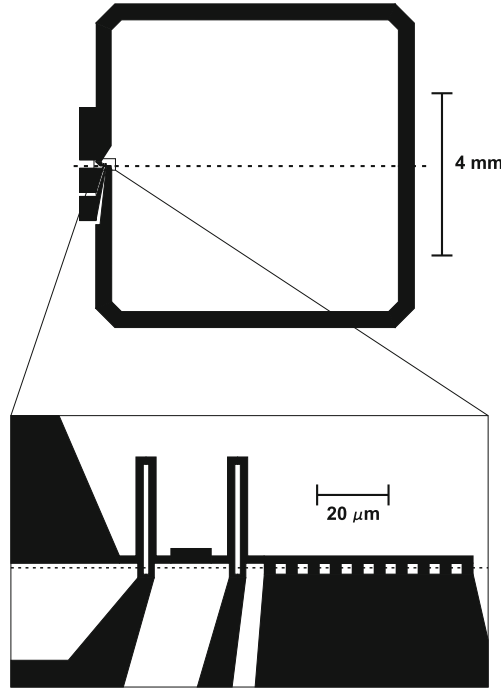


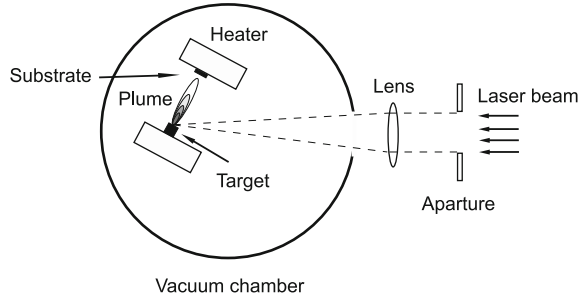
Fig. 2.9 Layout of the SQUID magnetometers. The large pick-up loop is $8 \times 8 \text{ mm}^2$ and incorporates flux dams shown in the zoomed up panel along with the two redundant hairpin SQUIDs. The *dashed line* indicates the grain boundary of the substrate

Table 2.1 A summary of the SQUID devices

Device	Baseline (mm)	Substrate(mm^3 STO)	Seed-layer	SQUID inductance(pH)
GRAD1	3	24° , $5 \times 10 \times 1$	—	46
GRAD2	4	24° , $10 \times 10 \times 1$	—	60
GRAD3	4	24° , $10 \times 10 \times 1$	—	60
GRAD4	4	24° , $10 \times 10 \times 1$	50 nm CeO_2	60
GRAD5	4	24° , $10 \times 10 \times 1$	50 nm CeO_2	60
GRAD6	4	24° , $10 \times 10 \times 1$	22 nm CeO_2	60
MAG1	—	24° , $10 \times 10 \times 1$	—	60
MAG2	—	30° , $10 \times 10 \times 0.5$	22 nm CeO_2	60
MAG3	—	30° , $10 \times 10 \times 0.5$	22 nm CeO_2	60
MAG4	—	24° , $10 \times 10 \times 1$	22 nm CeO_2	60
MAG5	—	24° , $10 \times 10 \times 0.5$	22 nm CeO_2	60

GRAD2-6. In order to limit the induced supercurrent in the pick-up loop, arrays of $6 \mu\text{m}$ Josephson junctions were incorporated in the pick-up loop where the thin film inevitably crosses the grain boundary. Furthermore, this prevents flux hopping in the

Fig. 2.10 A schematic drawing of a pulsed laser deposition system. The laser beam is defined by aperture before it is focused by a lens and enters the chamber where it hits a target. A plume is created by the ejected material from the target. The ejected material is deposited onto the heated substrate



weak parts on the grain boundary of the thin film, which reduces $1/f$ noise. A SQUID magnetometer was also applied for ULF-NMR/MRI (see Chap. 5). A summary of the devices can be found in Table 2.1. The SQUID inductances were extracted from simulations using the 3D-MLSI software [28, 31].

2.3 Device Fabrication

There are several types of practical high- T_c Josephson junctions but in this work YBCO bicrystal grain boundary type junctions have been used. Grain boundary Josephson junctions include, apart from bicrystalline junctions, biepitaxial and step-edge junctions [8, 32]. Examples of other types of junctions are constriction type, ion irradiation and ramp-edge type junctions [8, 33].

For the devices fabricated within this work, grain boundary bicrystal junctions have been utilized due to the reproducibility and simplicity to realize junctions. The bicrystal substrate is made from two SrTiO_3 (STO) single crystals bonded together at a misorientation angle of e.g. 24° or 30° . When an epitaxial thin film is deposited onto the substrate the grain boundary is transferred to the thin film creating a weak link with the same misorientation angle. Typical critical current densities (J_c) are on the order of 10^4 – 10^5 A/cm² for YBCO bicrystal junctions with a misorientation angle of 24° [32]. In most of the devices, as shown in Table 2.1, a seed-layer of CeO_2 was sputtered on the substrate before the YBCO thin film was grown. The seed layer is used to improve the quality of the YBCO thin film in the vicinity of the grain boundary of the substrate.

2.3.1 Thin Film Deposition

Deposition of YBCO thin films was made using pulsed laser deposition (PLD) which is a well established technique for growing high- T_c superconducting thin films. The

main advantage of PLD compared to other methods is the preservation of the stoichiometry (film composition) which is achieved by the short laser pulses used for target ablation. A disadvantage is formation of large clusters on the film surface. A review on PLD for YBCO deposition can be found in [34].

A schematic of a PLD system is shown in Fig. 2.10. A laser beam is defined by an aperture and focused by a lens before it enters the vacuum chamber. The laser pulses hit a polycrystalline YBCO target inside the chamber. A plasma plume is created by the ejected material from the target. The substrate is placed near the plume which enables the ejected material to be deposited on it.

The UHV-PLD system (DCA instruments) used for growing the thin films of YBCO for our devices consists of a Kr/F excimer laser from Lambda Physik with a wavelength of 248 nm and pulse duration of 20 ns, and a vacuum chamber containing a holder for the target and the substrate. The substrate holder can be set to rotate and/or scan during deposition in order to accomplish thin films on larger substrates (up to 2'') with homogeneous thickness. Heating is done via radiation from a SiC element. This type of heating gives a more homogeneous temperature of the sample compared to thermal heating where the sample is glued onto a heater. The PLD chamber is one part of a cluster system with a common transfer and loading system that enables deposition of oxides and metals in situ.

During thin film growth the substrate is located 51 mm from the target and is heated to around 810°C. The oxygen pressure during deposition is typically kept at 0.6–0.7 mbar. Finally, after the growth, the film is annealed in oxygen at 500–600°C for up to 120 min before it is cooled with a rate of 10°C/min. Thin films with thickness' of 200–350 nm and with T_c 's of about 90 K were grown for the devices described. After deposition, the YBCO is protected by a thin layer (~20 nm) of Au sputtered in situ.

The quality of YBCO thin films is of outmost importance for device fabrication [13]. It is desirable to achieve a high superconducting transition temperature and smooth films, however, they are typically complementary.

Transition Temperature

The transition temperatures of the thin films were determined by measuring the susceptibility of the superconducting film as a function of temperature. The setup consists of two coils with a small separation where the sample is placed. The mutual inductance of the coils is measured as the sample is cooled. At the transition temperature, the susceptibility of the superconductor changes and the mutual inductance between the two coils is altered due to screening currents in the superconductor.

The shape of the transition provides information about the quality of the thin film. It is desirable to achieve a high transition temperature with a narrow transition for optimum operation at 77 K. A representative transition temperature measurement of a YBCO thin film is shown in Fig. 2.11.

Fig. 2.11 Transition temperature measurement of a YBCO thin film deposited with PLD. The system measures the susceptibility (not calibrated, hence the arbitrary units) of the thin film as it is cooled to below its transition temperature

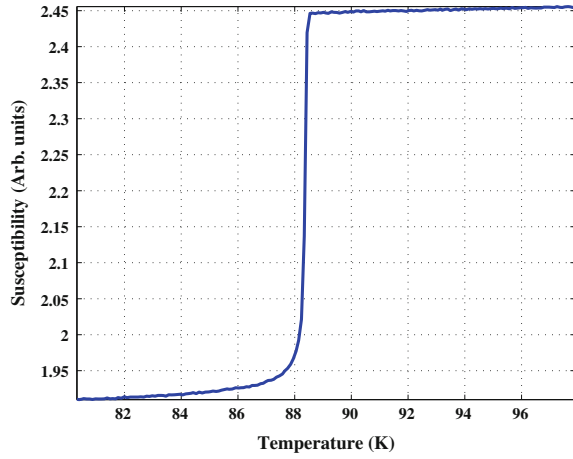
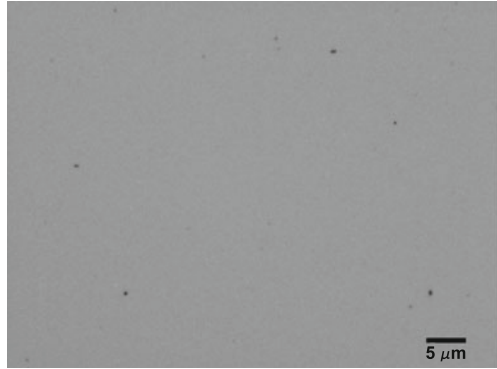


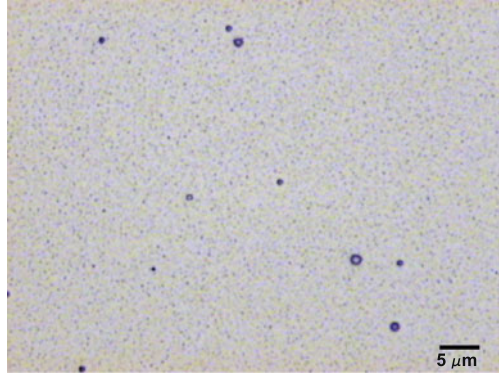
Fig. 2.12 A microscope photograph of a smooth YBCO thin film with few particles



Surface Morphology

The surface morphology of the thin films was investigated using an optical microscope. This method gives an indication of the surface quality in terms of particle density and smoothness and was sufficient for our purposes. A more thorough investigation of the surface morphology requires atomic force microscopy (AFM). Two optical microscope photographs of YBCO thin films on STO substrates are shown in Figs. 2.12 and 2.13. The YBCO thin film in Fig. 2.12 is an example of a smooth film with few particles whereas the thin film in Fig. 2.13 has more particles and is rougher.

Fig. 2.13 A microscope photograph of a rough YBCO thin film with some particles



2.3.2 Thin Film Processing

Patterning of the YBCO thin film was made with photolithography. A thin layer of UV sensitive photoresist (Shipley S1813) was spun onto the thin film. The photoresist was exposed to UV light ($\lambda = 400\text{ nm}$) through a chromium mask followed by development in MF-319. Argon ion milling was then used to etch the YBCO. The beam energy during etching was kept between 350 and 500 eV, and the current density to about $0.1\text{--}0.2\text{ mA/cm}^2$ in order to minimize the damage to the YBCO [13]. Gold pads were patterned using a lift-off process where windows in a layer of photoresist (S1813) were opened with photolithography. Under the S1813, a layer of LOR3A was spun and was used to achieve an undercut in order to facilitate the lift-off done in acetone and ultra-sound bath. The fabrication process is shown in a step-by-step manner in Fig. 2.14. A microscope photograph of GRAD1 is shown in Fig. 2.15.

2.4 SQUID Performance

The SQUID gradiometers were characterized in a shielded environment using a superconducting shield (Bismuth strontium calcium copper oxide, BSCCO) and mu-metal shielding but also unshielded which was particularly important for the immunoassay application. The magnetometers were characterized with a mu-metal shield and a superconducting shield or in the MEG setup inside a magnetically shielded room. For characterization of a SQUID it was glued onto a circuit-board and electrically connected with gold wire-bonds. In this dip-stick configuration, the SQUID was immersed in liquid nitrogen (77 K) either with a superconducting shield inserted into a copper tube covering the SQUID or with only the copper.

One of the fabricated gradiometers (GRAD1, Fig. 2.15) is presented in Paper I. The baseline of the gradiometer was 3 mm and the SQUID inductance was 46 pH. The SQUID on this $5 \times 10\text{ mm}^2$ large STO chip with a 24° misorientation angle had $3\text{ }\mu\text{m}$

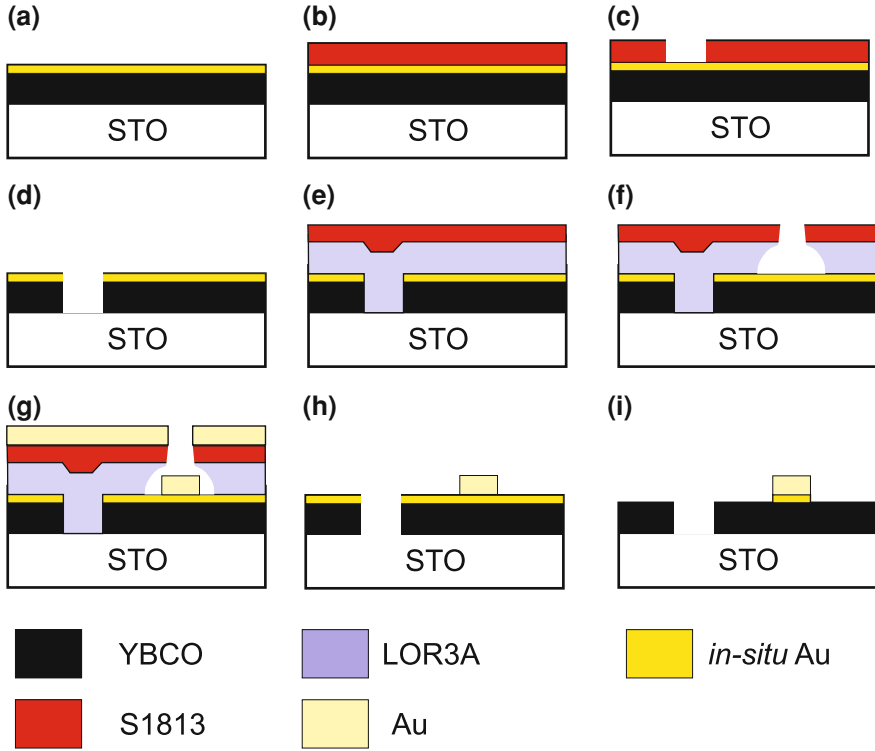


Fig. 2.14 A step-by-step description of the fabrication procedure (the figure is not to scale). **a** First, a YBCO thin film with thickness 200–350 nm is deposited onto a STO bicrystal substrate with an *in-situ* cap layer of Au (~20 nm). **b** A layer of photoresist (S1813) is spun onto the sample followed by baking on a hot plate (100°C for 1 min). **c** The photoresist is exposed by UV light through a chromium mask and developed in MF-319 followed by O₂ plasma etching. **d** Ar ion milling for about 120 min is used to etch the YBCO. **e** The next step is to fabricate gold pads which is done with a lift-off process. First, a layer of LOR3A is spun onto the sample followed by baking. Subsequently, a layer of photoresist (S1813) is applied to the sample. After exposure, the photoresist is developed in MF-319 followed by O₂ ashing. **f** Due to different development time of S1813 and LOR3A an undercut is achieved. **g–h** Sputtering of gold is followed by lift-off in acetone and ultra-sound bath. **i** Finally, the *in-situ* gold is removed with a few minutes of Ar ion milling

junctions with normal resistance, $R_n/2 = 1.3 \Omega$ and critical current $2I_c = 125 \mu\text{A}$ giving $I_c R_n = 170 \mu\text{V}$ at 77 K. The flux noise of GRAD1 is shown in Fig. 2.16 measured inside the superconducting shield with two different bias modes (dc and bias reversal). The flux noise at the white level was $4.6 \mu\Phi_0/\sqrt{\text{Hz}}$ and is comparable with the best achieved flux noise levels for high- T_c SQUIDs [36–40]. The well-balanced gradiometric configuration made operation in unshielded environments stable.

Two other gradiometers (GRAD2-3) had slightly larger baselines (4 mm) and the SQUID inductance was higher (60 pH). Flux modulated IV -curves of GRAD3 are

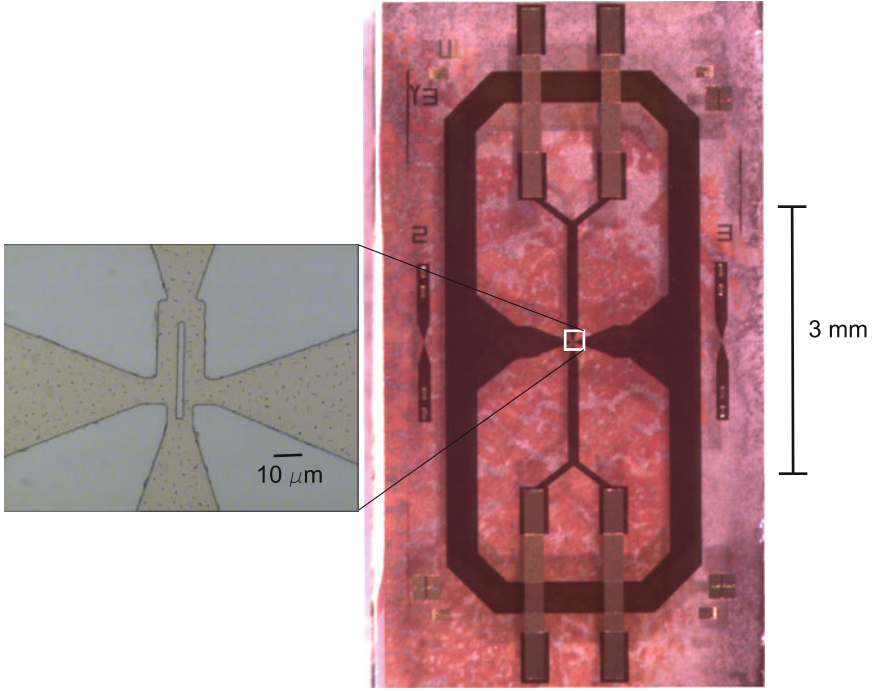


Fig. 2.15 Microscope photograph of GRAD1 and a close up of the hairpin SQUID. Adapted from [35]

Fig. 2.16 Flux noise of GRAD1 measured with shielding using bias reversal and dc bias. As can be seen, the low frequency noise is clearly suppressed by using bias reversal. Adapted from [35]

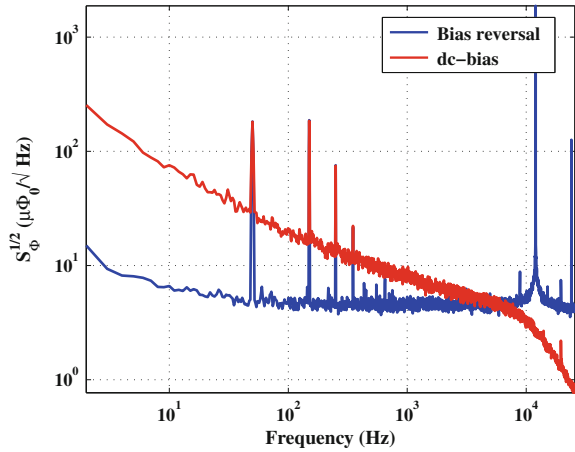


Fig. 2.17 Flux modulated I/V curves of GRAD3. The critical current at 77 K of $35\mu\text{A}$ is similar to GRAD2 on the same substrate. The normal resistance is 1Ω , giving $I_c R_n = 35\mu\text{V}$. The maximum voltage modulation is $10\mu\text{V}$

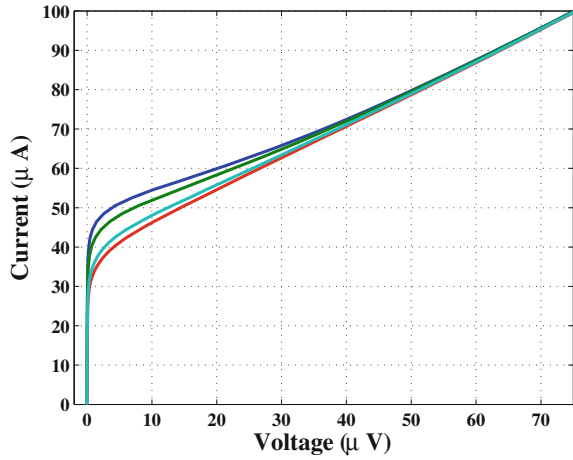
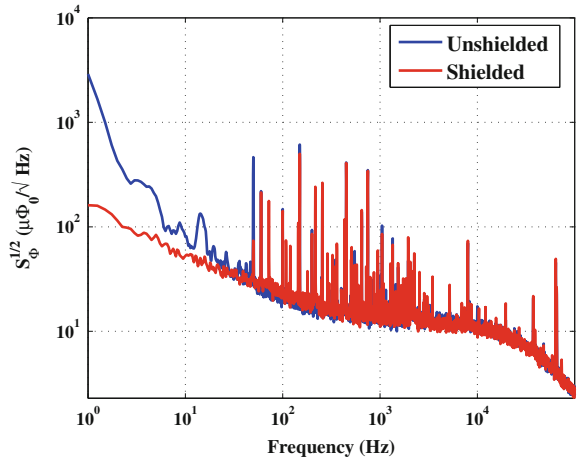


Fig. 2.18 Flux noise of GRAD3 measured with and without shielding with dc bias. The curves nearly overlap indicating that the gradiometer loops are well balanced. The flux noise at 1 kHz is $S_\Phi^{1/2} = 15\mu\Phi_0/\sqrt{\text{Hz}}$ with the $1/f$ knee at about 300 Hz



shown in Fig. 2.17. These two SQUIDs were fabricated on the same chip ($10\times 10\text{ mm}^2$ large STO chip with a 24° misorientation angle) and their properties were similar. The flux noise of GRAD3 measured in shielded and unshielded environments is shown in Fig. 2.18. Gradiometers 4-5 (GRAD4-5) were fabricated on a STO bicrystal (24° misorientation angle) substrate with a 50 nm CeO_2 seed-layer. The flux noise of the GRAD4 is shown in Fig. 2.19 measured with and without shielding with dc-bias and bias reversal. The critical current of this SQUID was $220\mu\text{A}$ with $I_c R_n = 176\mu\text{V}$, and the voltage modulation was $22\mu\text{V}$ at 77 K.

Lastly, GRAD6 was a single gradiometer on a $10\times 10\text{ mm}^2$ large STO chip with a 24° misorientation angle. The width of the junctions of the two redundant SQUIDs was $2\mu\text{m}$ and it had flux dams in the design (see Fig. 2.8). The noise of GRAD6L (the left SQUID) is shown in Fig. 2.20 measured in a shielded environment (mu-metal

Fig. 2.19 Flux noise of GRAD4 measured with and without shielding. The upper-most curves were measured using dc bias and the remaining two with bias reversal in order to reduce the $1/f$ noise

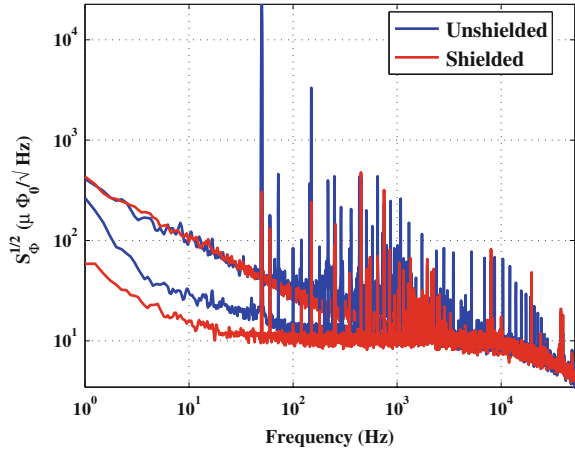
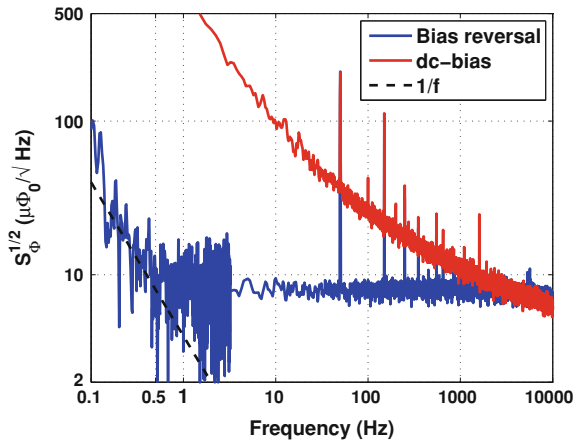


Fig. 2.20 Measured flux noise of GRAD6L with and without bias reversal in a superconducting shield. The $1/f$ -knee indicated by the dashed lines is at 0.5 Hz and the white noise level is $7.8 \mu\Phi_0/\sqrt{\text{Hz}}$



and superconducting shield). The $1/f$ -knee is at 0.5 Hz with bias reversal. This is among the best results reported for high- T_c SQUIDS. The low $1/f$ -knee with bias reversal shows the absence of trapped fluxes close to the SQUID body, and may be due to the small linewidths close to the SQUID and the presence of flux dams [41].

The most important feature of the magnetometers (MAG1-4, in Table 2.2) used for MEG is that they have low noise at low frequencies (1–20 Hz). The experiments conducted with the magnetometers were performed inside a magnetically shielded room (2 layers of mu-metal and one layer of copper coated aluminum). The SQUIDS were, for MEG recordings, operated with bias-reversal in order to reduce the $1/f$ -noise as much as possible. The flux noise of the magnetometer devices was typically $5\text{--}8 \mu\Phi_0/\sqrt{\text{Hz}}$ with the $1/f$ -knee below 10 Hz with bias reversal. In order to convert the flux noise to the equivalent magnetic field noise, a magnetic field calibration of the effective area was performed ($A_{eff} = \Phi_0/B$). A 40 cm diameter Helmholtz coil was

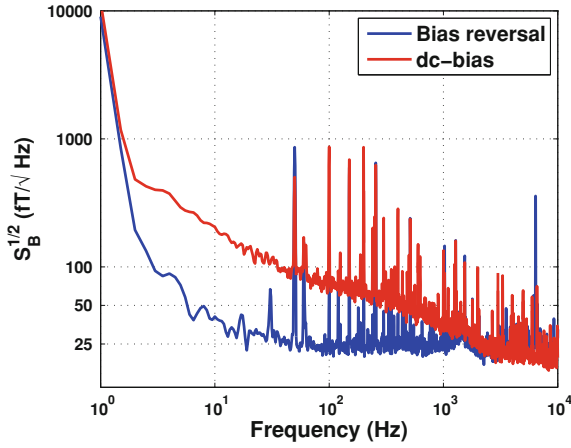


Fig. 2.21 The spectral density of equivalent magnetic field noise of MAG3R measured inside a magnetically shielded room in as the only shielding. The noise above 40 Hz is 25 and 43 fT/√Hz at 10 Hz with bias reversal

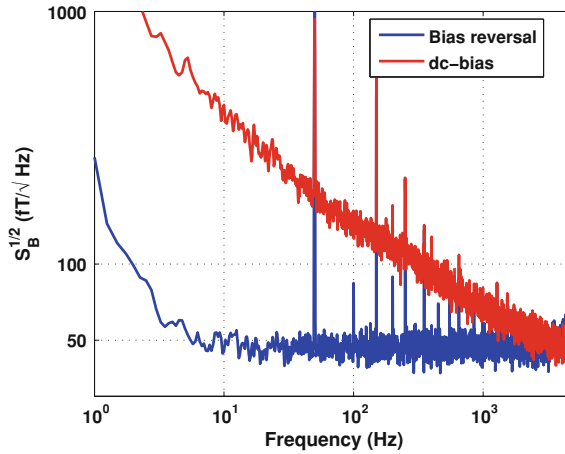


Fig. 2.22 The spectral density of equivalent magnetic field noise of MAG4L measured inside a magnetically shielded room in the MEG setup. The noise at 10 Hz is less than 50 fT/√Hz

placed such that the magnetic field lines were perpendicular to the magnetometer. It is important that the size of the coil is much larger than the sensor area to ensure a homogeneous field. The coil was well calibrated beforehand using a Hall probe magnetometer. The amplitude of the applied field was varied and the output of the SQUID (in FLL-mode) was noted. Finally, the output flux measured by the SQUID magnetometer was plotted against the applied field and with a straight line fit a conversion of $5.3 \text{ nT}/\Phi_0$ was obtained. Using the conversion, the magnetic field equivalent noise of two devices is shown in Figs. 2.21 and 2.22 (MAG3R and MAG4L

Table 2.2 A summary of properties of the SQUIDS measured at 77 K

Sample	L (pH)	$2I_c$ (μ A)	β_L	J_c (A/cm ²)	$R_n/2(\Omega)$	$I_c R_n$ (μ V)	ΔV (μ V)	$S_\Phi^{1/2}$ ($\mu\Phi_0/\sqrt{\text{Hz}}$)
GRAD1	46	125	2.9	10^4	1.3	170	41	4.6
GRAD2	60	35	1.0	4×10^3	1.1	39	11	10
GRAD3	60	35	1.0	4×10^3	1.0	35	10	15
GRAD4	60	220	6.4	1.3×10^4	0.8	176	22	10
GRAD5	60	205	6.0	1.2×10^4	1.0	205	25	9
GRAD6L	60	83	2.4	7×10^3	1.7	141	23	7.8
GRAD6R	60	105	3.0	8.8×10^3	—	—	17	7.5
MAG1L	60	7	0.2	4.3×10^2	8.0	56	30	6.1
MAG1R	60	1.5	0.04	92	14	21	21	80
MAG2L	60	40	1.2	2.5×10^3	2.0	80	30	8.3
MAG2R	60	80	2.4	5×10^3	1.6	128	32	—
MAG3L	60	5 ^a	0.15	3×10^2	10	50	33	5.7 ^b
MAG3R	60	5 ^a	0.15	3×10^2	9.2	46	50	4.7 ^b
MAG4L	60	80	2.3	4.4×10^3	2.0	160	28	8.2
MAG4R	60	50	1.5	2.8×10^3	2.2	110	32	7.3
MAG5L	60	180	5.2	10^4	—	—	15	12.5
MAG5R	60	80	2.3	4.4×10^3	1.0	80	16	12.5

The notation R and L indicates different SQUIDS on the same chip. The flux noise indicated was at above 1 kHz

^aTypical operation temperature below 77 K with critical current around 30 μ A

^bMeasured at ~ 74 K

respectively) measured in the MEG setup. In both devices, the $1/f$ -noise was reduced substantially with bias reversal. At 10 Hz the noise was about 50 fT/ $\sqrt{\text{Hz}}$ or less. In MAG3R, it reached down to 25 fT/ $\sqrt{\text{Hz}}$ above 40 Hz.

The characteristics of the SQUIDS are summarized in Table 2.2.

References

1. H.K. Onnes, The resistance of pure mercury at helium temperatures. Commun. Phys. Lab. Univ. Leiden, 12(120), (1911).
2. W. Meissner, R. Ochsenfeld, Naturwissenschaften **21**, 787 (1933)
3. L.N. Cooper, Bound electron pairs in a degenerate fermi gas. Phys. Rev. **104**(4), 1189–1190 (1956)
4. J.G. Bednorz, K.A. Müller, Possible high- T_c superconductivity in the Ba-La-Cu-O system. Z. Phys. B **62**(2), 189–193 (1996)
5. M.K. Wu, J.R. Ashburn, C.J. Torng, P.H. Hor, R.L. Meng, L. Gao, Z.J. Huang, Y.Q. Wang, C.W. Chu, Superconductivity at 93 K in a new mixed-phase Y-Ba-Cu-O compound system at ambient pressure. Phys. Rev. Lett. **58**, 908–910 (1987)
6. M. Tinkham, *Introduction to Superconductivity* (Dover publications, Mineola, 1996)
7. T. van Duzer, C.W. Turner, *Superconductive Devices and Electronics* (Prentice Hall PTR, New Jersey, 1999)
8. J. Clarke, A.I. Braginski, The SQUID handbook, vol. 1, (WILEY-VCH, Weinheim, 2006a).
9. J. Clarke, A.I. Braginski, *The SQUID handbook*, vol. 2 (WILEY-VCH, Weinheim, 2006b)

10. B.D. Josephson, Possible new effects in superconductive tunneling. *Phys Lett.* **1**(7), 251–253 (1962)
11. D.E. McCumber, Effect of ac impedance on dc voltage-current characteristics of superconductor weak-link junctions. *J. Appl. Phys.* **39**(7), 3113–3118 (1968)
12. W.C. Stewart, Current-voltage characteristics of josephson junctions. *Appl. Phys Lett.* **12**(8), 277–280 (1968)
13. D. Koelle, R. Kleiner, F. Ludwig, E. Dantsker, J. Clarke, High-transition-temperature superconducting quantum interference devices. *Rev. Mod. Phys.* **71**(3), 631–686 (1999)
14. K.K. Likharev, V.K. Semenov, Fluctuation spectrum in superconducting point junctions. *JETP Lett.* **15**(10), 625–629 (1972)
15. A.N. Vystavkin, V.N. Gubanov, L.S. Kuzmin, K.K. Likharev, V.V. Migulin, V.K. Semenov, S-c-S junctions as nonlinear elements of microwave receiving devices. *Phys. Rev. Appl.* **9**, 79 (1974)
16. J. Clarke, W.M. Goubau, M.B. Ketchen, Tunnel junction dc SQUID: Fabrication, operation, and performance. *J. Low Temp. Phys.* **25**, 99–144 (1976)
17. V. Ambegaokar, B.I. Halperin, Voltage due to thermal noise in the dc josephson effect. *Phys. Rev. Lett.* **22**, 1364–1366 (1969)
18. J. Clarke, R.H. Koch, The impact of high-temperature superconductivity on SQUIDs. *Science* **242**, 217–223 (1988)
19. R.H. Koch, J. Clarke, W.M. Goubau, J.M. Martinis, C.M. Pegrum, D.J. Van Harlingen, Flicker ($1/f$) noise in tunnel junction DC Squids. *J. Low Temp. Phys.* **51**(1–2), 207–224 (1983)
20. J. Clarke, G. Hawkins, Flicker ($1/f$) noise in Josephson tunnel junctions. *Phys. Rev. B* **14**(7), 2826–2831 (1976)
21. C.T. Rogers, R.A. Buhrman, Composition of $1/f$ noise in metal-insulator-metal tunnel junctions. *Phys. Rev. Lett.* **53**(13), 1272–1275 (1984)
22. D. Drung, High- T_c and low- T_c dc SQUID electronics. *Supercond. Sci. Technol.* **16**, 1320–1336 (2003)
23. E. Dantsker, S. Tanaka, J. Clarke, High- T_c superconducting quantum interference devices with slots of holes: Low $1/f$ noise in ambient magnetic fields. *Appl. Phys. Lett.* **70**(15), 2037–2039 (1997)
24. C.D. Tesche, J. Clarke, dc SQUID: Noise and optimization. *J. Low. Temp. Phys.* **29**(3–4), 301–331 (1977)
25. K. Enpuku, G. Tokita, T. Maruo, Inductance dependence of noise properties of a high- T_c dc superconducting quantum interference device. *J. Appl. Phys.* **76**(12), 8180–8185 (1994)
26. K. Enpuku, Y. Shimomura, T. Kisu, Effect of thermal noise on the characteristics of a high T_c dc superconducting quantum interference device. *J. Appl. Phys.* **73**(11), 7929–7934 (1993)
27. L.P. Lee, J. Longo, V. Vinetskiy, R. Cantor, Low noise $\text{YBa}_2\text{Cu}_3\text{O}_{7-\delta}$ direct-current superconducting quantum interference device magnetometer with direct signal injection. *Appl. Phys. Lett.* **66**(12), 1539–1541 (1995)
28. P. Magnelind, High- T_c SQUIDs for magnetophysiology, Ph.D. thesis, Chalmers University of Technology, 2006.
29. P.A. Rosenthal, M.R. Beasley, K. Char, M.S. Colclough, G. Zaharchuk, Flux focusing effects in planar thin-film grain-boundary Josephson junctions. *Appl. Phys. Lett.* **59**(26), 3482–3484 (1991)
30. M.B. Ketchen, J.M. Jaycox, Ultra-low-noise tunnel junction dc SQUID with a tightly coupled planar input coil. *Appl. Phys. Lett.* **40**(8), 736–738 (1982)
31. M.M. Khapaev, A. Yu. Kidiyarova-Shevchenko, P. Magnelind, M.Y. Kupriyanov. 3D-MLSI: Software package for inductance calculation in multilayer superconducting integrated circuits. *IEEE. Trans. Appl. Supercond.* **11**(1), 1090–1093 (2001)
32. H. Hilgenkamp, J. Mannhart, Grain boundaries in high- T_c superconductors. *Rev. Mod. Phys.* **74**, 485–549 (2002)
33. R. Gross, L. Alff, A. Beck, O.M. Froehlich, D. Koelle, A. Marx, Physics and technology of high temperature superconducting josephson junctions. *IEEE. Trans. Appl. Supercond.* **7**(2), 2929–2935 (1997)

34. R.K. Singh, D. Kumar, Pulsed laser deposition and characterization of high- T_c $\text{YBa}_2\text{Cu}_3\text{O}_{7-\delta}$. *Mater. Sci. Eng.* **22**, 113–185 (1997)
35. F. Öisjöen, P. Magnelind, A. Kalaboukhov, D. Winkler, High- T_c SQUID gradiometer system for immunoassays. *Supercond. Sci. Technol.* **2**, 034004 (4pp) (2008).
36. V. Schultze, D. Drung, R. Ijsselsteijn, H-G. Meyer, A high- T_c SQUID gradiometer with integrated homogeneous field compensation. *Supercond. Sci. Technol.* **17**, S165–S169 (2004)
37. P. Seidel, L. Dörrer, K. Peiselt, F. Schmidl, F. Smidth, C. Steigmeier, Development and investigation of novel single-layer gradiometers using highly balanced gradiometric SQUIDS. *Supercond. Sci. Technol.* **15**, 150–155 (2002)
38. K. Barthel, D. Koelle, B. Chesca, A.I. Braginski, A. Marx, R. Gross, R. Kleiner, Transfer function and thermal noise of $\text{YBa}_2\text{Cu}_3\text{O}_{7-\delta}$ direct current superconducting quantum interference devices operated under large thermal fluctuations. *Appl. Phys. Lett.* **74**(15), 2209–2211 (1999)
39. K. Enpuku, M. Hotta, A. Nakahodo, High- T_c SQUID system for biological immunoassays. *Physica C* **357–360**(1), 1462–1465 (2001b)
40. F. Ludwig, E. Dantsker, R. Kleiner, D. Koelle, J. Clarke, S. Knappe, D. Drung, H. Koch, N. McN, Alford, T.W. Button. Integrated high- T_c multiloop magnetometer. *Appl. Phys. Lett.* **66**(11), 1418–1412 (1995)
41. R.H. Koch, J.Z. Sun, V. Foglietta, W.J. Gallagher, Flux dam, a method to reduce extra low frequency noise when a superconducting magnetometer is exposed to a magnetic field. *Appl. Phys. Lett.* **67**, 709–711 (1995)

High-Tc SQUIDs for Biomedical Applications:
Immunoassays, Magnetoencephalography, and
Ultra-Low Field Magnetic Resonance Imaging

Öisjören, F.

2013, XVIII, 98 p., Hardcover

ISBN: 978-3-642-31355-4